Propylene polymerization and deactivation processes with isoselective cp/flu zirconocene catalysts

X. Desert, T. Roisnel, V. Dorcet, K. den Dauw, A. Vantomme, A. Welle, J.-F. Carpentier, E. Kirillov

catalysts

MDPI

Article

Propylene Polymerization and Deactivation Processes with Isoselective {Cp/Flu} Zirconocene Catalysts

Xavier Desert [1], Thierry Roisnel [2], Vincent Dorcet [2], Katty Den Dauw [3], Aurélien Vantomme [3], Alexandre Welle [3], Jean-François Carpentier [1,*] and Evgueni Kirillov [1,*]

1 Institut des Sciences Chimiques de Rennes (ISCR), Univ Rennes, CNRS, UMR 6226, F-35042 Rennes, France; desert.xavier@gmail.com
2 Centre de Diffraction X, ISCR (Institut des Sciences Chimiques de Rennes), Univ Rennes, CNRS, UMR 6226, F-35700 Rennes, France; thierry.roisnel@univ-rennes1.fr (T.R.); vincent.dorcet@univ-rennes1.fr (V.D.)
3 Total Research & Technology Feluy, Zone Industrielle Feluy C, B-7181 Seneffe, Belgium; katty.den-dauw@totalenergies.com (K.D.D.); aurelien.vantomme@totalenergies.com (A.V.); alexandre.welle@totalenergies.com (A.W.)
* Correspondence: jean-francois.carpentier@univ-rennes1.fr (J.-F.C.); evgueni.kirillov@univ-rennes1.fr (E.K.); Tel.: +33-223-236-118 (E.K.)

check for updates

Citation: Desert, X.; Roisnel, T.; Dorcet, V.; Den Dauw, K.; Vantomme, A.; Welle, A.; Carpentier, J.-F.; Kirillov, E. Propylene Polymerization and Deactivation Processes with Isoselective {Cp/Flu} Zirconocene Catalysts. *Catalysts* **2021**, *11*, 959. https://doi.org/10.3390/catal11080959

Academic Editors: Kotohiro Nomura, Takeshi Ohkuma, Martin Kotora, Alfonso Grassi, Victorio Cadierno, Carmine Capacchione, Ken-ichi Fujita, Kei Manabe, Raffaella Mancuso, Armando Pombeiro, Fabio Ragaini and Carl Redshaw

Received: 23 July 2021
Accepted: 7 August 2021
Published: 10 August 2021

Abstract: Industrially relevant single-site precatalysts used to produce isotactic polypropylene (iPP) include C_2-symmetric {SBI} and C_1-symmetric {Cp/Flu} complexes of group 4 metals. While the latter can produce iPPs with a higher degree of isotacticity, they also suffer from poor productivity compared to their {SBI} counterparts. Several causes for this trend have been suggested—2,1-Regioinsertions are frequently pointed out, as they are suspected to drive the catalyst into a dormant state. While this event does not seem to significantly impact the productivity of {SBI} systems, the influence of these regioerror is poorly documented for isoselective {Cp/Flu} precatalysts. To address this issue, new Ph_2X(Cp)(Flu) (Ph_2X = Ph_2C, FluC, Ph_2Si) proligands (**2a**–**k**) and some of the corresponding dichlorozirconocenes (**3a**–**h**,**k**) were synthesized. These new compounds were characterized and tested in homogeneous propylene polymerization at 60 °C and the amounts of regioerrors in the resulting polymers were examined by ^{13}C NMR spectroscopy. A possible correlation between poor productivity and a high number of regioerrors was investigated and is discussed. Furthermore, a C-H activation process in the bulky nBu$_3$C substituent upon activation of **4c** (the dimethylated analog of **3c**) by $B(C_6F_5)_3$ has been evidenced by NMR; DFT calculations support this C-H activation as a deactivation mechanism.

Keywords: zirconocene; polymerization; polypropylene; regiocontrol; stereocontrol; deactivation

1. Introduction

Since the development of isoselective polymerization of propylene with C_1-symmetric cyclopentadienyl-fluorenyl {Cp/Flu}-metallocene catalysts [1–4], many academic groups have set out to find "the" ideal structure that would produce polypropylene with the highest degree of isotacticity and regiocontrol, well-controlled molecular weight characteristics, and high productivity. This performance race has resulted in the synthesis of a vast number of structures with various substitution patterns [5–9], for the purpose of studying the influence of ligand architecture on the above parameters [10–12].

On the other hand, for the series of C_2-symmetric silicon-bridged *ansa*-bis(indenyl) or {SBI}-metallocene catalysts, significant breakthroughs have been achieved in the last decade, and a number of new structures have emerged that exhibit significantly improved performances (Scheme 1). Among them, of note are metallocene catalysts **A** [13–16] and **B** [17] that bear bulky aromatic 4-indenyl substituents and afford astonishing productivities, with highly crystalline iPP having remarkably low amounts of stereo- and regioerrors. Very recently, zirconocene catalyst **C**, which incorporates conformationally rigid tripticenyl

substituents, has been disclosed to be unprecedentedly efficient in terms of a range of relevant parameters: catalytic performance at high polymerization temperatures (up to 150 °C), stereocontrol (1 propylene misinsertion per 40,000 insertions at room temperature), and molecular weights (>10^6 g·mol^{-1}) [18].

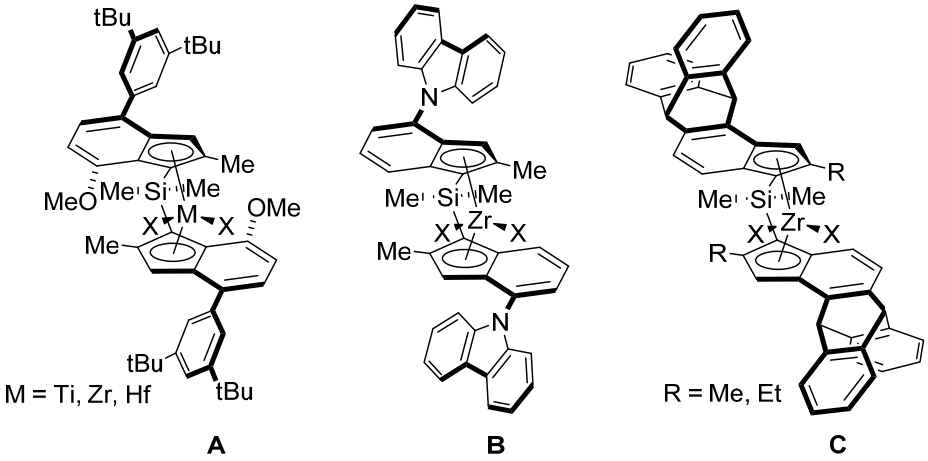

Scheme 1. Examples of highly performing C_2-symmetric {SBI}-metallocene catalysts.

In a previous contribution [19], we reported the possible origin of the differing productivity and behavior when comparing isoselective {SBI}- [20] and {Cp/Flu}-type [21–29] propylene polymerization precatalysts (Scheme 2). Indeed, the former catalysts are typically one order of magnitude more productive than the latter systems (15 × 10^4 kgPP·mol^{-1}·h^{-1} with **{SBI}-1** vs. 14 × 10^3 kgPP·mol^{-1}·h^{-1} with **{Cp/Flu}-1** at 60 °C and 5 bar), both under homogeneous and heterogeneous (supported) conditions. Yet, the kinetic data [19] unequivocally demonstrated that {Cp/Flu}-based systems (e.g., **{Cp/Flu}-2**) are intrinsically more active (in terms of propagation rates) and less prone to secondary (2,1-) propylene misinsertions than the {SBI}-systems. However, the very few resulting regiodefects appeared to be much more deleterious than for their {SBI} analogs.

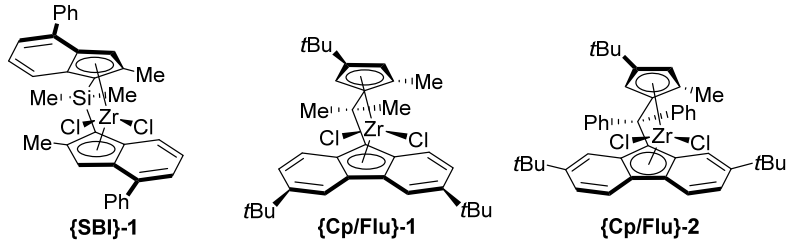

Scheme 2. Isoselective metallocene precursors for propylene polymerization.

In the present contribution, we aimed to extend the understanding of the impact of structural and/or electronic parameters on the regioselectivity of {Cp/Flu}-type isoselective catalytic systems, and decifer possible relationships between regiodefects and catalyst productivity. Thus, we considered a new series of modifications in order to: (1) vary the bulkiness of the 3-R-Cp substituents; (2) assess the impact of the nature and steric hindrance of the substituents in the 2,7- vs. 3,6-positions in the Flu platform; and (3) compare the constrained Ph_2C- vs. Ph_2Si-bridged {Cp/Flu} ligand platforms. This study also reports on the syntheses of these new precatalysts and their structural characterization both in solution and in the solid state. The performances of the new complexes were explored, after activation with MAO, in homogeneous propylene polymerization.

2. Results and Discussion

Syntheses of Proligands. In our previous studies [18–20], we used an efficient and scalable procedure for the synthesis of proligands {R^1R^2C-(Flu)(Cp)}H_2 via nucleophilic ad-

dition of substituted fluorenyl anions onto diversely multisubstituted fulvenes. Following this protocol, an extended series of new constrained $(aryl)_2C$-bridged proligands (**2a–j**) was here prepared in good yields (Scheme 3) and isolated as air-stable solids. The Ph_2Si-bridged **2k** was synthesized using a modified procedure reported for $\{R_2Si(Flu)(Cp)\}H_2$, where R = Me or Ph [30–34]. After optimization of the conditions and purification by column chromatography, proligand **2k** was isolated with an acceptable yield (47%) as a crystalline solid. Proligands **2a–k** were characterized by ^1H and ^{13}C NMR spectroscopy, ASAP mass-spectrometry, elemental analysis (see Protocol section in the Supporting Information), and X-ray crystallography (see the Supporting Information Figures S77–S87; Figure 1 for **2i**).

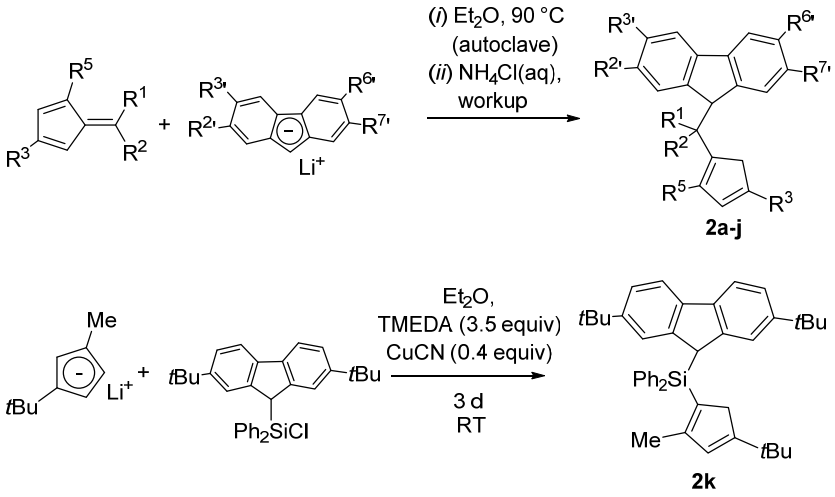

Bridge R^1, R^2	R^3	R^5	Fulvene	$R^{2'}$	$R^{3'}$	$R^{6'}$	$R^{7'}$	Proligand	Yield (%)
Ph_2C	*t*Bu	H	**1a**	*t*Bu	H	H	*t*Bu	**2a**	74
	$(Me_2tBu)C$	H	**1b**	*t*Bu	H	H	*t*Bu	**2b**	68
	$(n-Bu)_3C$	H	**1c**	*t*Bu	H	H	*t*Bu	**2c**	72
				H	*t*Bu	*t*Bu	H	**2d**	66
	(MeCy) [a]		**1e**	*t*Bu	H	H	*t*Bu	**2e**	63
	*t*Bu	H	**1a**	-$CMe_2CH_2CH_2CMe_2$- [b]				**2f**	78
				Cumyl	H	H	Cumyl	**2g**	41
	*t*Bu	Me	**1a-Me**	Mesityl	H	H	Mesityl	**2h**	48
1-FluC [c]	H	Me	**1i**	H	H	H	H	**2i**	44
	*t*Bu	H	**1j**	H	H	H	H	**2j**	20
Ph_2Si	*t*Bu	Me	**-**	*t*Bu	H	H	*t*Bu	**2k**	47

[a] R^3 = 1-methylcyclohexyl-; [b] 1,1,4,4,7,7,10,10-octamethy-l1,2,3,4,7,8,9,10-octahydrodibenzo[b,h]fluorene; [c] 5-5*H*-dibenzo[*b*,*d*]methylene.

Scheme 3. Synthesis of proligands: $(aryl)_2C$-bridged $\{(aryl)_2C$-$(Flu)(Cp)\}H_2$ **2a–j** and Ph_2Si-bridged **2k**.

Synthesis and Structure of Zirconocene Complexes. In order to prepare zirconocene dichlorides, regular salt metathesis reactions between anhydrous $ZrCl_4$ and ligands di-anions, generated in situ in Et_2O, were undertaken (Scheme 4). Thus, analytically pure zirconium complexes **3a–h** were isolated in reasonable yields after multiple crystallization attempts from heptane or heptane/CH_2Cl_2 mixtures as characteristically pink, microcrystalline materials. Following the same procedure, **3k** was isolated as a yellow microcrystalline powder. The low isolated yields found for some of the metallocene products resulted from multiple crystallization attempts undertaken to achieve the satisfactory purity needed for characterization and polymerization experiments.

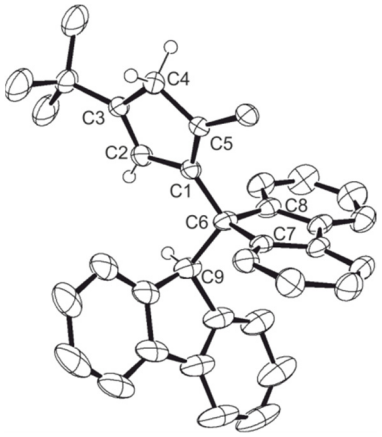

Figure 1. Crystal structure of proligand **2i** (H atoms except those of the 5-membered rings are omitted for clarity; ellipsoids are drawn at the 50% probability level).

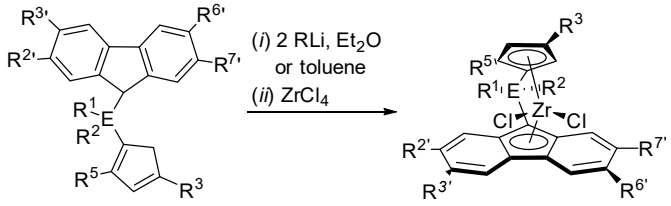

Bridge R^1, R^2	R^3	R^5	$R^{2'}$	$R^{3'}$	$R^{6'}$	$R^{7'}$	Proligand	Zr complex	Yield (%)
Ph_2C	*t*Bu	H	*t*Bu	H	H	*t*Bu	**2a**	**3a**	39
	$(Me_2tBu)C$	H	*t*Bu	H	H	*t*Bu	**2b**	**3b**	95
	$(n-Bu)_3C$	H	*t*Bu	H	H	*t*Bu	**2c**	**3c**	21
	(MeCy) [a]		H	*t*Bu	*t*Bu	H	**2d**	**3d**	8
	*t*Bu	H	*t*Bu	H	H	*t*Bu	**2e**	**3e**	22
			-$CMe_2CH_2CH_2CMe_2$- [b]				**2f**	**3f**	12
			Cumyl	H	H	Cumyl	**2g**	**3g**	12
	*t*Bu	Me	Mesityl	H	H	Mesityl	**2h**	**3h**	48
FluC [c]	H	H	H	H	H	H	**2i**	-	-
	*t*Bu	H	H	H	H	H	**2j**	-	-
Ph_2Si	*t*Bu	Me	*t*Bu	H	H	*t*Bu	**2k**	**3k**	23

[a] R^3 = 1-methylcyclohexyl-; [b] 1,1,4,4,7,7,10,10-octamethy-l1,2,3,4,7,8,9,10-octahydrodibenzo[b,h]fluorene; [c] 5-5*H*-dibenzo[*b*,*d*]methylene.

Scheme 4. Synthesis of *ansa*-zirconocenes **3a–h** and **3k**.

Despite numerous attempts, the respective zirconium complexes derived from proligands **2i** and **2j** could not be isolated using the standard conditions shown in Scheme 4. Even upon using the conditions reported for the synthesis of complexes {FluC(3-*t*Bu-Cp)$_2$}$ZrCl_2$ and {FluC(Cp)$_2$}$ZrCl_2$ incorporating the same FluC bridge (deprotonation of the proligands with *n*BuLi at −40 °C, followed by the salt-metathesis reaction with $ZrCl_4$ at −70 °C in CH_2Cl_2 and then under stirring for 2 h at −20 °C, see [35]), these experiments did not result in the isolation of the desired complexes, and complex mixtures of unidentified products were systematically obtained.

The solution structures of **3a**–**h** and **3k** were studied using ^{1}H and ^{13}C NMR spectroscopy and were found to be consistent with the C_1-symmetry of these species. Analysis of the ^{13}C NMR data (see Figures S45, S47, S49, S51, S53, S55, S58, S60, S62 and S64 in the Supporting Information) revealed particularly upfield *C*9-fluorenyl carbon signals (δ_C

74.5–80.8 ppm), which is indicative of a reduced coordination hapticity ($\eta^5 \rightarrow \eta^3$) of the fluorenyl ligands maintained in solution [36,37]. The iASAP-MS spectra for most of the complexes are also available in the Supporting Information (Figures S72–S79).

Single crystals of **3b**–**e**,**g** and **h** suitable for X-ray diffraction studies (Figures 2–7) were grown from CH_2Cl_2/*n*-hexane (1:1 *v*/*v*) solutions at room temperature. In the solid state, the molecules exhibited geometrical parameters (Table 1) essentially similar to those observed in a series of similar zirconocene dichlorides incorporating R_2C-bridged {Cp/Flu} ligands described by our group (e.g., {Ph_2C(3,6-*t*Bu_2-Flu)(3-*t*Bu-Cp)}$ZrCl_2$ (**{Cp/Flu}^{5H}**)) [12,25–27] and several others [2,7–9,38–40]. The coordination of the central five-membered ring of the fluorenyl ligand in most complexes deviated slightly from η^5 towards η^3, as revealed by the differences in the Zr–C(ring) distances (*ca.* 0.3 Å between the shortest and the longest bond lengths); this is consistent with the above comment in solution. The Cp_{cent}–Zr–Flu_{cent} bite angles were found in a rather narrow range of values (116.85–118.61°) and were similar to the corresponding values in the Ph_2C-bridged metallocene **{Cp/Flu}^{5H}** (118.03°) [25].

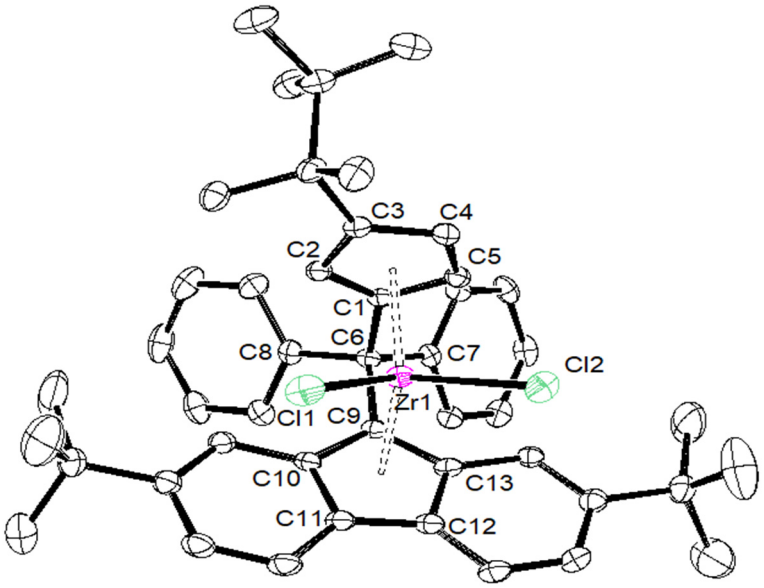

Figure 2. Crystal structure of complex **3b** (hydrogen atoms are omitted for clarity; ellipsoids are drawn at the 50% probability level).

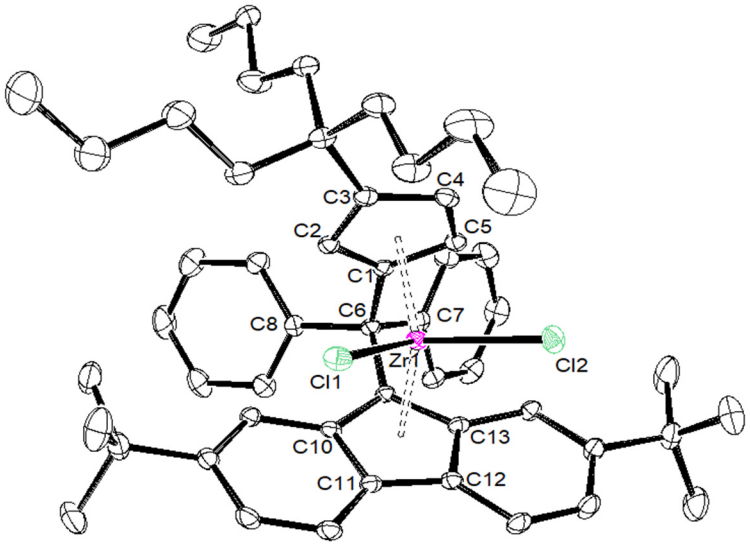

Figure 3. Crystal structure of complex **3c**·CH_2Cl_2 (hydrogen atoms and CH_2Cl_2 are omitted for clarity; ellipsoids are drawn at the 50% probability level).

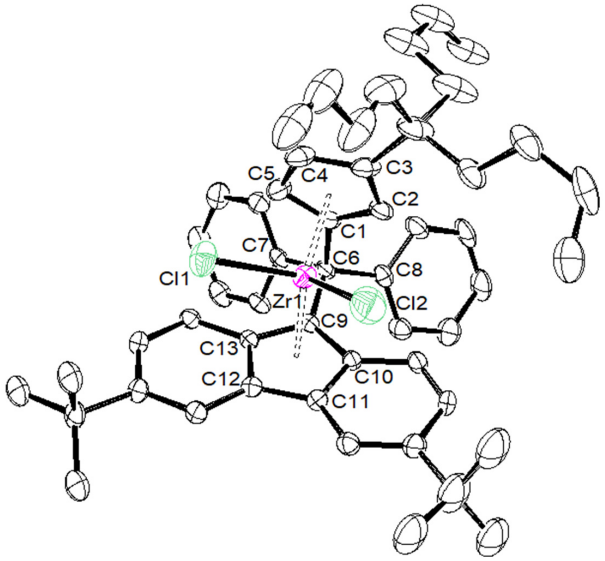

Figure 4. Crystal structure of complex **3d** (hydrogen atoms are omitted for clarity; ellipsoids are drawn at the 50% probability level).

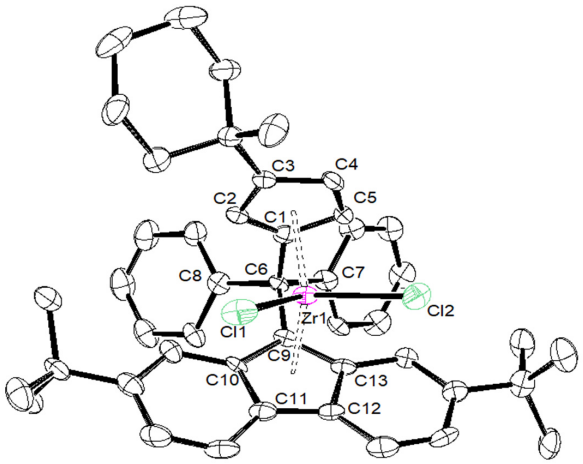

Figure 5. Crystal structure of complex **3e** (hydrogen atoms are omitted for clarity; ellipsoids are drawn at the 50% probability level).

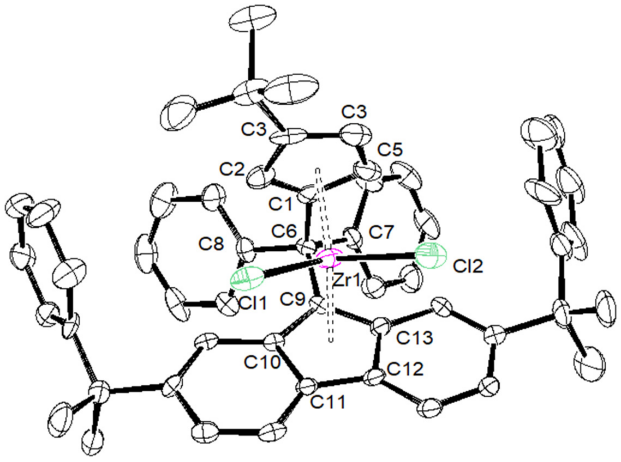

Figure 6. Crystal structure of complex **3g** (hydrogen atoms are omitted for clarity; ellipsoids are drawn at the 50% probability level).

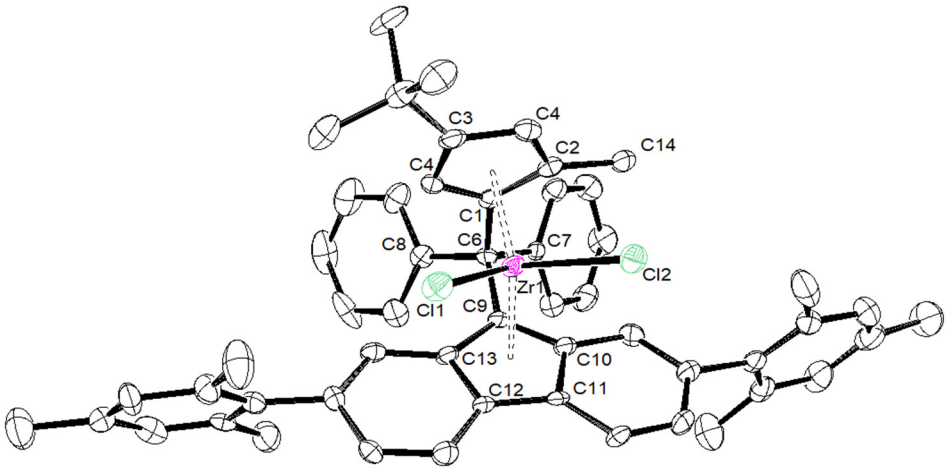

Figure 7. Crystal structure of complex **3h**·$(C_6H_{14})_{0.5}$ (hydrogen atoms and hexane are omitted for clarity; ellipsoids are drawn at the 50% probability level).

Table 1. Selected bond lengths (Å) and angles (°) for metallocene complexes **3b**–**e**, **g** and **h**.

	{Cp/Flu}^{5H}	3b	3c	3d	3e	3g	3h
Zr–C(1)	2.442 (4)	2.4450 (17)	2.4391 (14)	2.451 (4)	2.443 (8)	2.440 (5)	2.442 (6)
Zr–C(2)	2.492 (3)	2.4745 (18)	2.4720 (15)	2.484 (4)	2.489 (8)	2.459 (5)	2.468 (6)
Zr–C(3)	2.630 (4)	2.6079 (18)	2.6431 (15)	2.645 (4)	2.594 (8)	2.582 (5)	2.587 (6)
Zr–C(4)	2.547 (4)	2.5284 (18)	2.5706 (15)	2.558 (4)	2.514 (8)	2.554 (6)	2.525 (6)
Zr–C(5)	2.457 (4)	2.4384 (18)	2.4408 (15)	2.433 (4)	2.429 (8)	2.463 (5)	2.459 (6)
Zr–Cp_{cent}	2.204	2.242	2.204	2.209	2.180	2.190	2.181
Zr–C(9)	2.426 (3)	2.4108 (18)	2.4229 (15)	2.445 (4)	2.403 (8)	2.407 (5)	2.420 (6)
Zr–C(10)	2.497 (4)	2.5128 (18)	2.5020 (15)	2.510 (4)	2.500 (8)	2.505 (5)	2.488 (6)
Zr–C(11)	2.666 (4)	2.6740 (18)	2.6621 (15)	2.683 (4)	2.686 (8)	2.681 (5)	2.695 (6)
Zr–C(12)	2.712 (4)	2.6633 (18)	2.6732 (15)	2.707 (4)	2.670 (8)	2.688 (5)	2.660 (6)
Zr–C(13)	2.588 (4)	2.5083 (18)	2.5263 (15)	2.552 (4)	2.514 (8)	2.524 (4)	2.563 (6)
Zr–Flu_{cent}	2.269	2.188	2.240	2.272	2.245	2.250	2.256
Cp_{cent}–Zr–Flu_{cent}	118.03	118.15	117.80	116.85	117.93	118.45	118.61
C(1)–C(6)–C(9)	98.60 (3)	99.13 (14)	98.73 (11)	99.20 (3)	99.10 (6)	99.20 (6)	100.10 (5)
C(7)–C(6)–C(8)	104.00 (4)	104.33 (14)	104.82 (12)	105.60 (3)	104.30 (7)	104.50 (4)	101.10 (5)

Propylene polymerization. *Ansa*-metallocenes **3a**–**h**,**k**, in combination with MAO, were evaluated in the propylene polymerization (toluene solution, 5 bar constant pressure, T_{pol} = 60–100 °C). Each polymerization experiment was independently repeated three times under the same conditions, revealing good reproducibility in terms of the activity (gas uptake), productivity (polymer yield), and physicochemical properties (M_w, M_n, T_m, isotacticity) of the isolated polymer. For benchmarking purposes, the performance of the reference zirconocene **{Cp/Flu}-2** (Scheme 2) was explored under identical conditions. Due to a high exothermicity at $[Zr]_0$ = 10.0 μM, the polymerization experiments with **{Cp/Flu}-2** were conducted at lower concentrations (5.0 μM). Selected polymerization results are summarized in Table 2 (and reported in Table S3).

Several trends could be specifically drawn. However, these activity data should be considered with care, since the polymerization reactions carried out with highly active systems, such as that based on **{Cp/Flu}-2**, were quite exothermic, even with low precatalyst loadings. As a result, the temperature of the reaction mixtures could hardly be controlled, often outreaching configured values after a few minutes (see Table 2). The trends evidenced the flexibility and limits of the polymerization processes with these catalytic systems:

- The most active precatalyst within the given series of propylene polymerization precatalysts appeared to be the reference metallocene **{Cp/Flu}-2**. For instance, in a

typical experiment performed at 60 °C (entry 1), the productivity of the latter catalyst was found to be 1.5–10 times higher (50,700 kg PP·mol^{-1}·h^{-1}) than those observed for all other precursors (up to 35,500 kg PP·mol^{-1}·h^{-1}).

- The second by productivity (35,500 kg PP·mol^{-1}·h^{-1}) appeared to be the less sterically constrained system incorporating **3a**, which is analogous to **{Cp/Flu}-2** but has no Me substituent at the position 5 of the Cp ligand.
- Increasing the bulkiness of the 3-R substituent at the Cp ligand (R = *t*BuMe$_2$C in **3b** and R = 1-methylcyclohexyl in **3e**) resulted in a significant drop in productivity (5300 kg PP·mol^{-1}·h^{-1} and 16,700 kg PP·mol^{-1}·h^{-1}; entries 3 and 7, respectively). At the same time, metallocene systems **3c** and **3d**, both incorporating the bulky aliphatic 3-*n*Bu$_3$C substituent at the Cp ligand, were unexpectedly found to be very poorly or completely inactive (entries 4 and 5, respectively). The latter result can stem from deactivation involving a *n*Bu group of the 3-*n*Bu$_3$C substituent (vide infra).
- Keeping the 3-*t*Bu substituent at the Cp ligand while altering the nature of the 2,7-/3,6-substituents also resulted in catalysts featuring inferior productivities. Thus, **3f**–**3h** afforded comparable productivities in the range of 12,700–17,200 kg PP·mol^{-1}·h^{-1} (entries 8–10).
- Regarding the molecular weights of the PPs produced, all active systems yielded similar products, with M_n lying in the range of 11.4–24.9 kg·mol^{-1}, showing no specific trend and being lower than that of the PP obtained with the reference metallocene catalyst **{Cp/Flu}-2** (50.7 kg·mol^{-1}). The polydispersity values (PDI = 2.1–2.5) were all consistent with the single-site behavior of these catalyst systems.
- The stereoregularities of the PPs obtained from {Cp/Flu}-based catalysts can vary over a broad range, depending on the substituents both on the Cp and Flu moieties [10,11,18–20]. The new metallocenes with bulky 3-R substituents on the Cp ligand (**3a**,**b**,**e**) afforded polypropylenes featuring pentad [*m*]^4 values (86.2–88.6%) higher than those observed with **{Cp/Flu}-2** (82.1%). These stereoregularity levels are also reflected in the corresponding T_m values determined for these polymers (139.8–141.1 vs. 131.1, respectively). The highest stereoselectivity ([*m*]^4 = 91.2%) within the series was achieved with metallocene catalyst **3f** with the 2,3,6,7-tetra-substituted version of fluorenyl ligand (Oct), which afforded PP with T_m of 148.4.
- Being the 2,7-Mes$_2$-Flu-substituted analogue of **{Cp/Flu}-2**, system **3h** quite unexpectedly afforded PP with a low isotacticity index ([*m*]^4 = 54.0%; see the Supporting Information Table S4). This result cannot be explained by the higher bulkiness of the mesityl substituents.
- The incorporation of a Si-bridge (entry 11) appeared to confer a negative effect on all parameters (productivity, molecular weight, stereoregularity (Table S4), and T_m), as evidenced upon comparing the results obtained with **3k** and its Ph$_2$C-bridged analogue **{Cp/Flu}-2**. In order to improve the productivity, a polymerization experiment was conducted at 100 °C (entry 12), but it resulted in an almost total loss of activity; this possibly reflects significant deactivation or even degradation of the catalyst at this temperature. The viscous material recovered from these attempts was found to be a mixture of oligomers exhibiting no melting transition. In a previous contribution, Chen and Rausch et al. [30] explained that the loss of syndioselectivity and poorer productivity of {Me$_2$Si(Flu)(Cp)}ZrCl$_2$ with respect to the Me$_2$C-bridged congener were due to steric hindrance of metal center. Thus, the larger Cp$_{cent}$-Si-Flu$_{cent}$ bite angle, which is ca. 10° greater than that in the carbon-bridged counterpart, makes the coordination sphere both less accessible and less selective towards the coordination of monomer.

Table 2. Propylene polymerization experiments [a].

Entry	Precat.	T_{polym} [b]	Prod ($kg^{PP} \cdot mol \cdot h^{-1}$)	T_m (°C) [c]	T_{cryst} [c] (°C)	M_n [d] ($\times 10^3$)	M_w/M_n [d]	$[m]^4$ [e] (%)	1,2-ins [e] (%)	2,1-ins [e] (%)	1,3-ins [e] (%)	*n*Bu termini [e] (%)
1	**{Cp/Flu}-2**	60 (68)	50,700 [f]	131.1	93.6	50.8	2.5	82.1	99.8	<0.02	0.1	0.1
2	**3a**	60 (66)	35,500	135.8	102.6	11.4	2.1	86.5	99.3	<0.1	0.3	0.2
3	**3b**	60 (65)	5300	141.1	106.2	15.4	2.1	88.6	99.2	0.2	0.4	0.3
4	**3c**	60 (65)	241	137.1	106.2	-	-	-	-	-	-	-
5	**3d**	60 (64)	0	-	-	-	-	-	-	-	-	-
6	**3e**	60 (76)	33,600	132.9	100.3	13.7	2.1	81.6	99.3	<0.02	0.3	0.04
7		60 (67)	16,700 [g]	139.8	104.5	21.7	2.1	86.2	99.5	<0.1	0.3	≈0.1
8	**3f**	60 (66)	13,300	148.4	112.6	17.6	2.3	91.7	99.6	<0.02	0.1	< 0.1
9	**3g**	60 (66)	12,700	136.1	102.3	21.0	2.3	82.9	99.4	0.1	0.3	0.1
10	**3h**	60 (68)	17,200	n.o.	n.o.	24.9	2.1	54.0	99.7	<0.02	0.1	<0.02
11	**3k**	60 (64)	1870	131.7	119.8	13.4	2.2	31.9	99.6	<0.02	<0.01	<0.02
12		100 (102)	640	n.o.	n.o.	3.4	1.4	-	-	-	-	-

[a] Polymerization conditions, otherwise stated: 300 mL high-pressure glass reactor; solvent: toluene, 150 mL; P (propylene) = 5 bar; Tpolym = 60 °C, [Zr]0 = 10.0 μM, [Al]/[Zr] = 5000; n.o. = not observed. [b] Data in brackets refer to the maximum temperature reached in the reactor. [c] Determined by DSC. [d] Determined by GPC/SEC. [e] Determined by ^{13}C NMR spectroscopy. [f] [Zr]0 = 5.0 μM, [Al]/[Zr] = 10,000. [g] [Zr]0 = 5.0 μM , [Al]/[Zr] = 5000.

Influence of metallocene structure on regioselectivity. The deactivation of $MgCl_2$-supported Ziegler–Natta catalyst systems used for propylene polymerization via 2,1-misinsertions and reactivation of their dormant state by the deliberate introduction of H_2 as a chain-transfer agent (CTA) have been reported by Cipullo et al. [41]. In our previous contribution [19], we established a marked impact of regioirregular (2,1-, secondary) insertions on the stability and activity of propagating species in the polymerization of propylene with {Cp/Flu}-based systems. In the latter case, the formation of "dormant" Zr–*sec*-alkyl species by 2,1-misinsertion of the α-olefin (Scheme 5), reluctant to further insertions, has been also shown to have a critical role for deactivation process. The existence of Zr–*sec*-alkyl species can be indirectly evidenced from the ^{13}C NMR spectroscopic data with the presence of head-head and tail-tail sequences in the resulting polymer. The presence of *n*Bu chain-ends in the polymers, resulting from protonolysis (transfer to H_2 or acidic hydrolysis) of "dormant" Zr–*sec*-alkyl species, can be hence considered as a fingerprint of massive deactivation of the catalyst. The reorganization of "dormant" Zr–*sec*-alkyl species though a multistep process (1,3-insertion) [42,43] comprising a β-H elimination reaction from the methyl group of the ultimate unit and then 1,2-reinsertion of the σ-olefin obtained in the previous step, could constitute a re-activation process resulting in restitution of catalytic activity (Scheme 5).

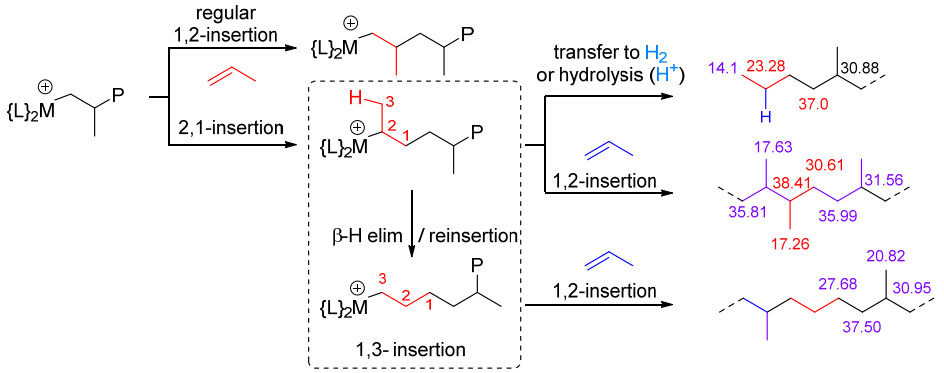

Scheme 5. Possible propylene insertion pathways and ^{13}C NMR spectroscopic fingerprints of the chain-ends and sequences resulting from regioirregular insertions of propylene [44–47].

On attempting to find out the connection between the lower productivities of some {Cp/Flu}-based systems and their propensity towards affording regioirregular insertions, a closer inspection of the $^{13}C\{^1H\}$ NMR spectra of the PPs produced with **3a–c**,**e–h** and the reference system **{Cp/Flu}-2** was carried out (Table 2). For a more complete set of data, a complementary analysis was conducted with the polymers obtained with some previously reported analogous {Cp/Flu}-based systems (Scheme 6; Table 3, entries 1–7) [11,25–27]. The respective resonances derived from the 2,1- and 1,3-insertions and those from the terminal *n*Bu chain-ends were identified, quantified, and used to plot the combined bar diagram (Figure 8). Yet, regrettably, no correlation could be identified between the productivity and the content of the titled sequences from regioirregular insertions or *n*Bu chain-ends. Nevertheless, it appears that minor changes (e.g., **3b** or **3a** vs. **{Cp/Flu}-2**) in the {Cp/Flu}-metallocene structure can induce dramatic effects on regio- and stereo-control as well as on productivity.

In striking contrast with the {Cp/Flu}-systems, the {SBI}-based counterparts feature a much higher propensity towards affording 2,1- and 1,3-insertions, thus resulting in much larger contents of the corresponding regioerrors (Table 3, entries 8 and 9), which are apparently not deleterious for the productivity of these systems. In fact, in that case, the M–*sec*-alkyl species are still reactive and capable of either undergoing further regular 1,2-insertions of propylene or regenerating an active hydrido species upon β-H elimination [19].

Table 3. Propylene polymerization data obtained with precatalysts from Scheme 6 [a].

Entry	Precat.	$[Zr]_0$ ($\mu mol.L^{-1}$)	[Al/[Zr]	Prod ($kg^{PP} \cdot mol \cdot h^{-1}$)	$[m]^4$ [b] (%)	1,2-ins [b] (%)	2,1-ins [b] (%)	1,3-ins [b] (%)	*n*Bu Termini [b] (%)
1	**{Cp/Flu}-1**	10.0	5000	1100	90.5	99.8	<0.02	0.1	<0.02
2	**{Cp/Flu}-3^{Me}**	10.0	5000	15,470	88.1	99.8	<0.02	<0.1	<0.02
3	**{Cp/Flu}-3^{Et}**	10.0	5000	9730	89.5	99.8	<0.02	<0.1	<0.02
4	**{Cp/Flu}-3^{Ph}**	20.0	5000	2000	53.8	99.5	<0.02	<0.01	<0.02
5	**{Cp/Flu}-4^{Me}**	10.0	5000	29,600	90.7	99.8	<0.02	0.02	<0.02
6	**{Cp/Flu}-4^{Et}**	10.0	5000	26,260	90.8	99.7	<0.02	0.02	<0.02
7	**{Cp/Flu}-5**	10.0	5000	1550	80.9	99.6	<0.02	0.09	0.2
8	**{SBI}-1**	2.0	25,000	62,700	93.6	98.6	0.26	0.5	0.05
9	**{SBI}-2**	2.0	25,000	27,900	83.4	99.2	0.45	0.05	<0.1

[a] Polymerization conditions, otherwise stated: 300 mL high-pressure glass reactor; solvent: toluene, 150 mL; P (propylene) = 5 bar; T_{polym} = 60 °C. [b] Determined by ^{13}C NMR spectroscopy.

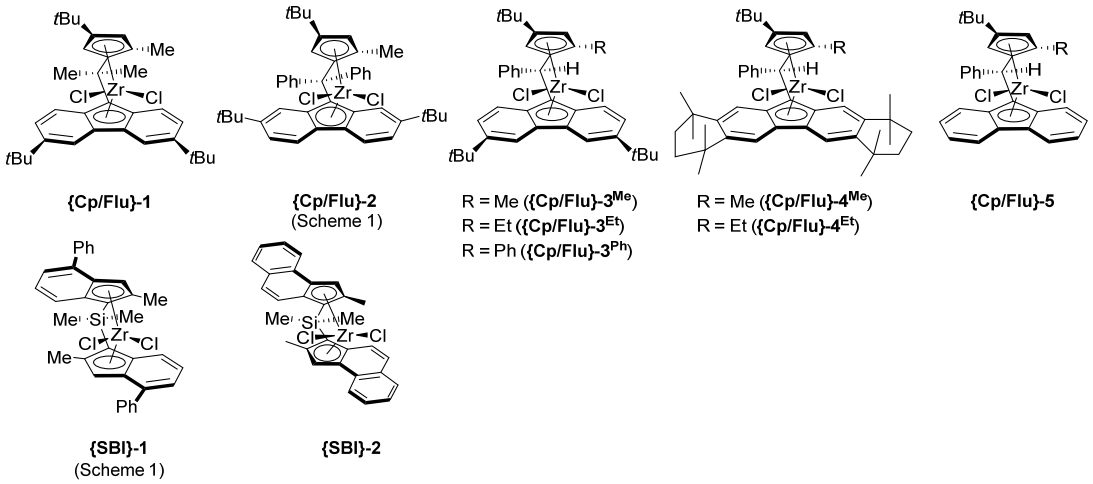

Scheme 6. Structures of precatalysts used for benchmarking.

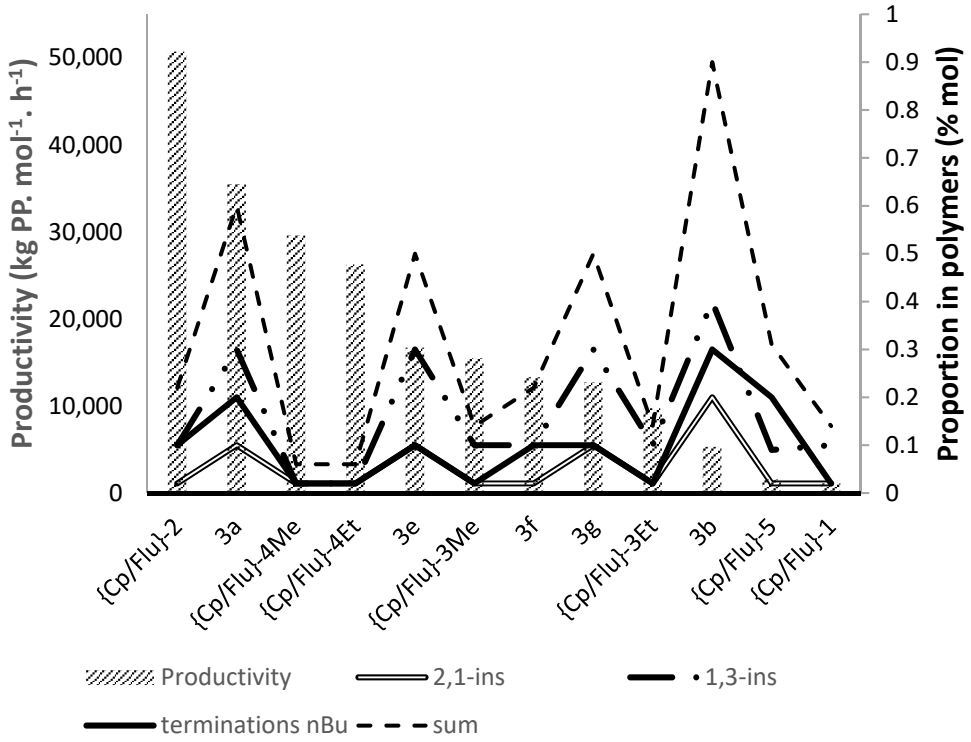

Figure 8. Productivity of the {Cp/Flu}-based catalytic systems and extent of regiodefects in PP samples.

Deactivation of the catalytic system based on 3c. Complexes {Ph_2C(2,7-$t$$Bu_2$-Flu)(3-$n$$Bu_3$C-Cp)}$ZrCl_2$ (**3c**) and {Ph_2C(3,6-$t$$Bu_2$-Flu)(3-$n$$Bu_3$C-Cp)}$ZrCl_2$ (**3d**), in combination with MAO, showed particularly low productivity in the polymerization of propylene that could not be rationalized on the basis of steric factors. To address this phenomenon, we aimed at understanding the role of activation conditions as well as of ion-pairing effects. The introduction of excess MAO necessary for the activation of **3c** is likely to generate a complex NMR spectrum that would not allow for observing all the phenomena involved, especially in the aliphatic region. Therefore, the generation of the corresponding ion pair was carried out upon using molecular activators such as $B(C_6F_5)_3$ [27].

The dimethyl-zirconocene **4c** was selectively prepared from the parent **3c** by a reaction with 2 equiv. of Grignard's MeMgBr (see SI). Further treatment of **4c** with 1 equiv. of

$B(C_6F_5)_3$, carried out on an NMR scale in toluene-d_8 at −50 °C, resulted in quantitative and selective generation of the corresponding ion-pair **4c-MeB(C$_6$F$_5$)$_3$** (Scheme 7). All attempts to grow crystals of **4c-MeB(C$_6$F$_5$)$_3$** failed thus far. The ^{1}H NMR spectrum recorded at this temperature (Figure 9a) showed the complete disappearance of the Zr–Me signals (δ_H −1.09 and −0.99 ppm) and the appearance of two equal intensity resonances at δ_H −0.38 and −0.22 ppm corresponding to the Zr–Me and B–Me groups, respectively. The ion pair **4c-MeB(C$_6$F$_5$)$_3$** was found stable in the temperature range of −50–+10 °C and was characterized by multinuclear NMR spectroscopy. For example, the ^{1}H and ^{13}C{^{1}H} NMR spectra of **4c-MeB(C$_6$F$_5$)$_3$**, recorded at −50 °C (Figures S65 and S66, respectively), each contained a single set of signals. Furthermore, the difference in the chemical shifts of the *meta*- and *para*-F resonances, $|\Delta\delta$ (*m*,*p*-F)$|$ = 4.8 ppm in the ^{19}F{^{1}H} NMR spectrum of **4c-MeB(C$_6$F$_5$)$_3$**, is in agreement with the inner-sphere ion-pairing (ISIP) nature of that species. Typically, the corresponding $|\Delta\delta$ (*m*,*p*-F)$|$ values for ISIPs are greater than 3.5 ppm, while those for OSIPs are smaller than 3.0 ppm; see: [48]. This observation is consistent with the fact that this ion pair exists as a single isomer, in which the coordinated $MeB(C_6F_5)_3^-$ anion occupies the less hindered lateral coordination site [28,29]. This is in contrast with less bulky ion-pair analogues derived from similar C_1-symmetric metallocenes, which consist of mixtures of two isomers that feature different coordination of the $MeB(C_6F_5)_3^-$ anion (in the more open and the less hindered lateral coordination site, respectively).

Above 15 °C, a new series of signals appeared in the ^{1}H NMR spectrum (Figure 9b), evidencing a new species whose formation was accompanied by concomitant formation of methane (δ_H 0.19 ppm). The reaction was completed after 24 h at room temperature, and the recorded ^{1}H NMR spectrum contained only one new series of resonances (Figure 9c). Close inspection of the aliphatic region of this ^{1}H NMR spectrum allowed for the identification of the nature of the product—the new cationic Zr–alkyl complex **5c-MeB(C$_6$F$_5$)$_3$** formed by an intramolecular C–H activation reaction (Scheme 7) between one *n*Bu group and Zr–Me, eventually releasing 1 equiv. of methane. Among the three possible products **A**–**C** arising from a C–H activation site in the alkyl chain of the *n*Bu group, the selective formation of regioisomer **C** took place as judged from the NMR data. Additional 2D (COSY, HSQC) NMR spectroscopic techniques allowed for a proper assignment of all signals (Figures S70 and S71). The Zr–(2-(2-ethyl)ethyl) fragment appears in the ^{1}H NMR spectrum (Figure 9c) as a set of characteristic signals: a multiplet (δ_H −1.62 ppm) for the methine hydrogen H^c (Zr–C*H*), two multiplets (δ_H 0.01 and 1.41 ppm) for the diastereotopic hydrogens H^b and H$^{b'}$ (C*HH*CH$_3$), a triplet (δ_H 0.36 ppm; $^3J_{H\text{-}H}$ = 7.0 Hz) for the hydrogens H^a (C*H*$_3$), and a triplet (δ_H 1.74 ppm; $^3J_{H\text{-}H}$ = 14.0 Hz) and a doublet of doublets (δ_H 2.45 ppm; $^2J_{H\text{-}H}$ = 6.5 Hz, $^3J_{H\text{-}H}$ = 14.0 Hz) for the diastereotopic hydrogens H^d and H$^{d'}$ (−CC*HH*CH–Zr). In the ^{13}C{^{1}H} NMR spectrum, four distinct resonances are observed, including a distinctive one for the metallated carbon (Figure S70) [49]: δ_C 80.6 (Zr–CH), 32.0 (CH_2CH_3), 17.1 (CH_2CH_3), and 59.5 (−CCH_2CH–Zr) ppm. Furthermore, in the ^{19}F{^{1}H} NMR spectrum of **5c-MeB(C$_6$F$_5$)$_3$** (Figure S69), the difference in the chemical shifts of the *meta*- and *para*-F resonances, $|\Delta\delta$ (*m*,*p*-F)$|$ = 5.0 ppm, is in line with the ISIP nature of this species [48].

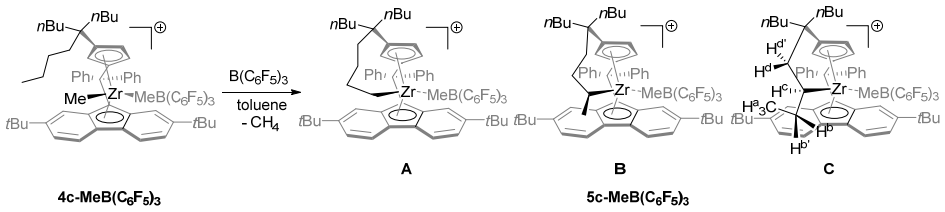

Scheme 7. Formation of **5c-MeB(C$_6$F$_5$)$_3$** (possible isomers **A**–**C**) by intramolecular C-H activation from **4c-MeB(C$_6$F$_5$)$_3$**.

Based on the above results, we surmised that a similar rapid deactivation process is operational with **3c** and **3d** in the presence of MAO, thus affording at some point very

stable sterically congested ion pairs with [Me-MAO]$^-$ anions, which are further reluctant towards reactions with propylene.

Theoretical studies of a possible deactivation pathway. To gain further insight into this deactivation phenomenon, DFT calculations were conducted using as model the putative cationic methyl-zirconocene complex [**4c-Me**]$^+$ (Scheme 8) obtained upon activation with MAO or $B(C_6F_5)_3$, namely [{Ph_2C(2,7-$t$$Bu_2$Flu)(3-$n$$Bu_3$-$C_5H_2$)}Zr–Me]$^+$ (B3PW91 level, see the Supporting Information for details). The objectives of these non-exhaustive computations were to assess the total electronic energy profiles for two possible concurrent processes, that is: (a) regular coordination/insertion of propylene into the Zr–Me bond of [**4c-Me**]$^+$ to give the respective insertion species [**4c-iBu**]$^+$, vs. (b) intramolecular C-H activation in the pendant $n$$Bu_3$C group by the cationic metal center generating metallacyclic species (most possible isomers B and C, Scheme 7), and consecutive reactions of the latter species with propylene. Despite metallocene species with fully substituted Cp and Flu rings were considered in the computations, some simplifications/assumptions were made to reduce the calculation costs: (i) the influence of the counter anion was disregarded, and only "naked" cationic species were considered; and (ii) the methyl or *iso*-butyl group (representing the polymeryl chain) resides in the opposite direction to the bulky $n$$Bu_3$C substituent. In addition, when reactions with propylene were conceived, it was assumed that (iii) the insertion of propylene proceeds in a primary ("pr") fashion, and (iv) finally, as usually considered for isospecific polymerization of propylene mediated by C_1-symmetric {Cp/Flu}-metallocene catalysts, the molecule of monomer coordinates to the cationic zirconium center with its methyl group positioned "head down" into the free space in the central region of the fluorenyl ligand, while the methylene group is directed toward the less-congested quadrant (opposite to the methyl or *iso*-butyl groups/polymeryl chain).

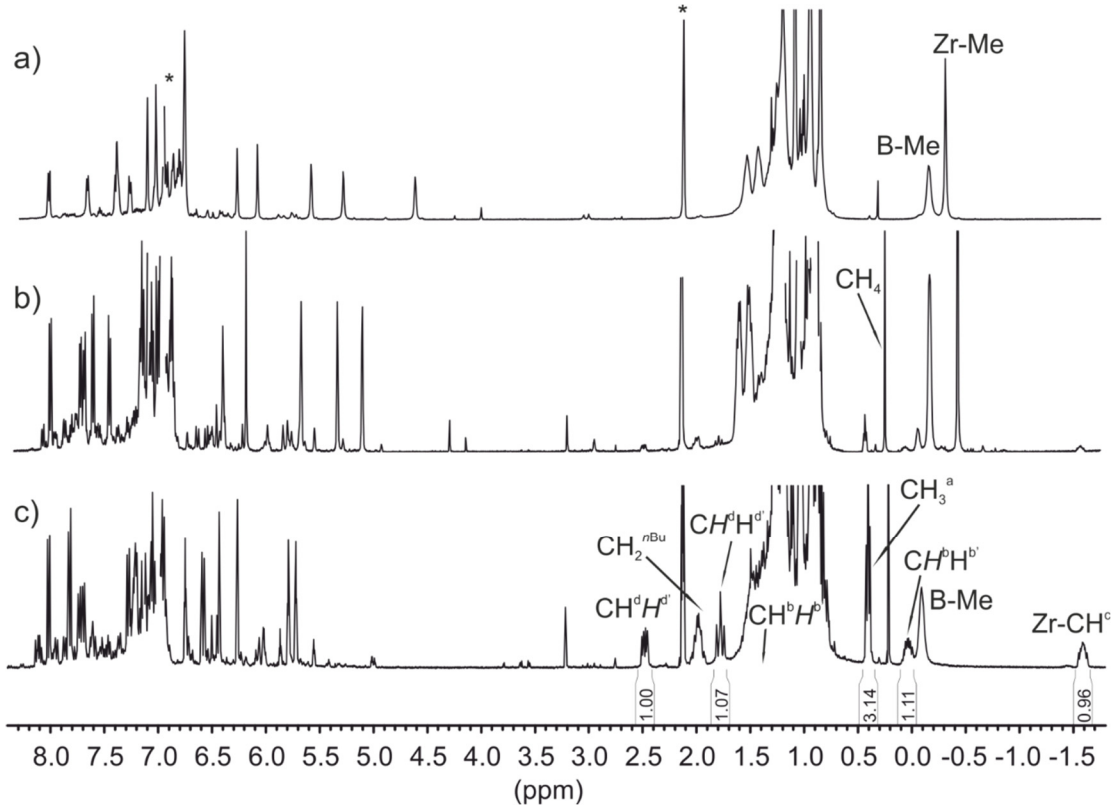

Figure 9. ^{1}H NMR spectra (500 MHz, toluene-d_8) of the reaction between **4c** and $B(C_6F_5)_3$ (1:1) recorded progressively after: (**a**) 10 min at −50 °C; (**b**) 10 min at 15 °C; and (**c**) 24 h at RT, yielding isomer **C** (Scheme 7) of **5c-MeB(C_6F_5)$_3$**. * stands for residual solvent (toluene-d_8) signals.

The regular propagation pathway was assessed at the first insertion step, that is, conversion of the π-complex [**4c-Me**]$^+$ (Scheme 8) to isobutyl species [**4c-iBu**]$^+$. As expected, this process was found to be favorable on both kinetic and thermodynamic grounds, showing the reasonable calculated activation barrier $\Delta E^{\neq}_{\mathbf{TS1}\,prsi}$ = 12.1 kcal·mol^{-1} for the primary insertion of propylene with *si* face, which should result in isotactic polymer. Barriers in the range 7.1–8.6 and 10.0–15.0 kcal·mol^{-1} for the first and second primary insertions of propylene into the Zr–C bond, respectively, were calculated for the cationic species [{$R^1{}_2C$(3,6-*t*Bu_2Flu)(3-*t*Bu-5-R^2-C_5H_2)}Zr–(polymeryl)]$^+$ (R^1 = H, Ph; R^2 = Me, Ph); see reference [10].

The metallation (C–H activation) of the *n*Bu group in the *n*Bu_3C substituent, requiring a proximal Zr–R function and accompanied by a concomitant alkane (methane or *iso*-butane) elimination, was computed to occur through somewhat higher but still accessible transition states both for R = Me in [**4c-Me**]$^+$ ($\Delta E^{\neq}_{\mathbf{TS2}}$ = 19.7 and 20.2 kcal·mol^{-1}) and for R = *i*Bu in [**4c-iBu**]$^+$ species ($\Delta E^{\neq}_{\mathbf{TS2'}}$ = 18.4 and 19.4 kcal·mol^{-1}). While the C–H activation reaction from [**4c-iBu**]$^+$ species was computed to be essentially endothermic (8.7 and 6.5 kcal·mol^{-1}), the same process from [**4c-Me**]$^+$ species appeared to be thermodynamically favored (−3.9 and −1.7 kcal·mol^{-1}). This suggests that the C–H activation phenomenon leading to isomers B and C can preferably occur for the cationic complex initially formed at the precatalyst activation stage and, especially, in the absence of propylene. In line with the experimental results, the formation of isomer C was found computationally to be more favored both kinetically ($\Delta\Delta E^{\neq}$ = 0.5–1.0 kcal·mol^{-1}) and thermodynamically ($\Delta\Delta E$ = 2.2 kcal·mol^{-1}), regardless the nature of [**4c-R**]$^+$ precursor. Further propylene insertions in the metallacyclic isomers B and C (to give the corresponding products **P**) were computed to be favored thermodynamically (ΔE = −11.4–−5.5 kcal·mol^{-1}), and connected through accessible transition states ($\Delta E^{\neq}$ = 12.9–17.3 kcal·mol^{-1}).

These results indicate that the formation of metallacyclic species by intramolecular C–H activation is a smooth process and likely to take place during the very first steps of polymerization. However, this process seems to be not deleterious for the posterior reactivity with propylene and could lead to the formation of larger metallacyclic propagating species. Apparently, deactivation takes effect on later steps through a series of intramolecular C–H activation processes successively involving all the *n*Bu groups of the *n*Bu_3C substituent and eventually resulting in a steric obstruction of the active site.

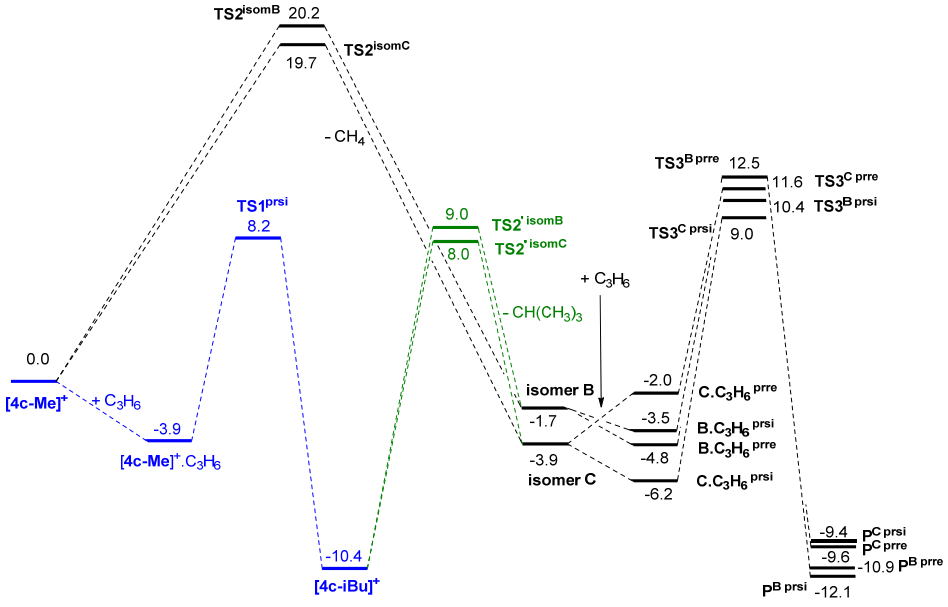

Scheme 8. Energy profiles computed at the B3PW91 level for propylene coordination/insertion and possible decomposition routes for active species generated from the [**4c-Me**]$^+$ cation (energies in kcal·mol^{-1} relative to [**4c-Me**]$^+$ + propylene).

3. Conclusions

New se C_1-symmetric *ansa*-zirconocenes with multisubstituted $\{R_2E\text{-}(Flu)(Cp)\}^{2-}$ ligands were prepared. In most cases, the activation of these complexes with MAO gave highly active and isoselective propylene polymerization catalytic systems. The highest productivity, comparable to that of the **{Cp/Flu}-2** reference system, was observed with **3a** and **3e**, with both incorporating bulky 3-R-Cp substituents ($tBuCMe_2C$ and MeCy, respectively). The complete inactivity of the 3-nBu$_3$C-Cp substituted **3c** and **3d** in propylene polymerization was rationalized from NMR spectroscopic studies on a model system incorporating the $[\mathbf{4c}]^+[MeB(C_6F_5)_3]$ ion pair and from DFT calculations. Both indicated a concurrent decomposition route involving intramolecular C-H activation in the nBu$_3$C-groups. The most isoselective system within the whole series appeared to be **3f**, bearing an octamethyloctahydrodibenzofluorenyl-based ligand. Quite unexpectedly, the 2,7-Mes_2-Flu substitution in **3h** appeared to be detrimental for stereocontrol and resulted in much poorer isotacticity. The impact of different substitution patterns on the occurrence of regioerrors involving both 2,1- and 1,3-insertions was sought in this study. However, no distinct correlation could be identified thus far between them nor between the observed productivities and the content of the regioirregular sequences in the obtained polymers. Further investigations aimed at clarifying the origin of the different catalytic behaviors among this series of metallocene catalysts are underway in our laboratories.

Supplementary Materials: The following are available online at https://www.mdpi.com/article/10.3390/catal11080959/s1—Materials and Methods, Figure S1: ^{1}H NMR ($CDCl_3$, 400 MHz, 25 °C) of 6-methyl-6′-tert-butylfulvene. Figure S2: $^{13}C\{^1H\}$ NMR spectrum ($CDCl_3$, 100 MHz, 25 °C) of 6-methyl-6′-tert-butylfulvene (mixture of isomers). Figure S3: ^{1}H NMR spectrum (CD_2Cl_2, 400 MHz, 25 °C) of 2-(2,3,3-trimethylbutan-2-yl)cyclopentadiene (mixture of isomers). Figure S4: $^{13}C\{^1H\}$ NMR spectrum (CD_2Cl_2, 100 MHz, 25 °C) of 2-(2,3,3-trimethylbutan-2-yl)cyclopentadiene (mixture of isomers). Figure S5: ^{1}H NMR spectrum (CD_2Cl_2, 400 MHz, 25 °C) of fulvene **1b**. Figure S6: $^{13}C\{^1H\}$ NMR spectrum (CD_2Cl_2, 100 MHz, 25 °C) of fulvene **1b**. Figure S7: ^{1}H NMR spectrum ($CDCl_3$, 400 MHz, 25°C) of 1-(tri-n-butyl)-cyclopentadiene (mixture of isomers). Figure S8: $^{13}C\{^1H\}$ NMR spectrum ($CDCl_3$, 100 MHz, 25 °C) of 1-(tri-n-butyl)-cyclopentadiene (mixture of isomers). Figure S9: ^{1}H NMR spectrum (CD_2Cl_2, 400 MHz, 25 °C) of **1c**. Figure S10: $^{13}C\{^1H\}$ NMR spectrum (CD_2Cl_2, 100 MHz, 25 °C) of **1c**. Figure S11: ^{1}H NMR spectrum (CDCl3, 400 MHz, 25 °C) of 1-(methyl-cyclohexyl)-cyclopentadiene (mixture of isomers). Figure S12: 13C{1H} NMR spectrum (CDCl3, 100 MHz, 25 °C) of 1-(methyl-cyclohexyl)-cyclopentadiene. Figure S13: ^{1}H NMR spectrum (CDCl3, 400 MHz, 25 °C) of 1e. Figure S14: 13C{1H} NMR spectrum (CDCl3, 100 MHz, 25 °C) of 1e. Figure S15: ^{1}H NMR spectrum (CD2Cl2, 400 MHz, 25 °C) of **1i**. Figure S16: 13C{1H} NMR spectrum (CD2Cl2, 100 MHz, 25 °C) of 1i. Figure S17: ^{1}H NMR spectrum (CD2Cl2, 400 MHz, 25 °C) of **1j**. Figure S18: 13C{1H} NMR spectrum (CD2Cl2, 100 MHz, 25 °C) of **1j**. Figure S19: ^{1}H NMR spectrum (CD2Cl2, 400 MHz, 25 °C) of 2a. Figure S20: 13C{1H} NMR spectrum (CD2Cl2, 100 MHz, 25 °C) of 2a. Figure S21: ^{1}H NMR spectrum (CD2Cl2, 400 MHz, 25 °C) of 2b. Figure S22: 13C{1H} NMR spectrum (CD2Cl2, 100 MHz, 25 °C) of 2b. Figure S23. 13C{1H} NMR JMOD experiment (CD2Cl2, 100 MHz, 25 °C) of 2b. Figure S24: ^{1}H NMR spectrum (CD2Cl2, 400 MHz, 25 °C) of **2c**. Figure S25: 13C{1H} NMR spectrum (CD2Cl2, 100 MHz, 25 °C) of 2c. Figure S26: 13C{1H}NMR JMOD spectrum (CD2Cl2, 100 MHz, 25 °C) of 2c. Figure S27: ^{1}H NMR spectrum (CD2Cl2, 400 MHz, 25 °C) of **2d**. Figure S28: 13C{1H} NMR spectrum (CD2Cl2, 100 MHz, 25 °C) of 2d. Figure S29: 13C DEPT135 experiment (CD2Cl2, 100 MHz, 25 °C) of 2d. Figure S30: ^{1}H NMR spectrum (CD2Cl2, 400 MHz, 25 °C) of 2e. * stands for residual NMR solvent signal. Figure S31: 13C{1H} NMR spectrum (CD2Cl2, 100 MHz, 25 °C) of 2e. Figure S32: ^{1}H NMR spectrum (CD2Cl2, 400 MHz, 25 °C) of 2f. * stands for residual NMR solvent signal. Figure S33: 13C{1H} NMR spectrum (CD2Cl2, 100 MHz, 25 °C) of 2f. Figure S34: ^{1}H NMR spectrum (CD2Cl2, 400 MHz, 25 °C) of 2g. Figure S35: 13C{1H} NMR spectrum (CD2Cl2, 100 MHz, 25 °C) of 2g. Figure S36: ^{1}H NMR spectrum (CD2Cl2, 100 MHz, 25 °C) of 2h. * stands for residual NMR solvent signal. Figure S37: 13C{1H} NMR spectrum (CD2Cl2, 100 MHz, 25 °C) of 2h. Figure S38: ^{1}H NMR spectrum (CD2Cl2, 400 MHz, 25 °C) of **2i**, Figure S39: 13C{1H} NMR spectrum (CD2Cl2, 100 MHz, 25 °C) of 2i. Figure S40: ^{1}H NMR spectrum (CD2Cl2, 400 MHz, 25 °C) of 2j. Figure S41: 13C{1H} NMR spectrum (CD2Cl2, 100 MHz, 25 °C) of 2j. Figure S42: ^{1}H NMR spectrum (CD2Cl2, 400 MHz, 25 °C) of 2k. Figure S43: 13C{1H} NMR spectrum (CD2Cl2, 100 MHz, 25 °C)

of 2k. Figure S44: ^{1}H NMR spectrum (CD2Cl2, 400 MHz, 25 °C) of 3a. Figure S45: 13C{1H} NMR spectrum (CD2Cl2, 100 MHz, 25 °C) of 3a. Figure S46: ^{1}H NMR spectrum (CD2Cl2, 400 MHz, 25 °C) of 3b. Figure S47. 13C{1H} NMR spectrum (CD2Cl2, 100 MHz, 25 °C) of 3b. Figure S48: ^{1}H NMR spectrum (CD2Cl2, 400 MHz, 25 °C) of 3c. Figure S49: 13C{1H} NMR spectrum (CD2Cl2, 100 MHz, 25 °C) of 3c. Figure S50: ^{1}H NMR spectrum (C6D6, 500 MHz, 25 °C) of 3c-Me. Figure S51: 13C{1H} NMR spectrum (CD2Cl2, 125 MHz, 25 °C) of 3c-Me. Figure S52: ^{1}H NMR spectrum (C6D6, 400 MHz, 25 °C) of 3d. Figure S53: 13C{1H} NMR spectrum (C6D6, 100 MHz, 25 °C) of 3d. Figure S54: ^{1}H NMR spectrum (C6D6, 500 MHz, 25 °C) of 3e. Figure S55: 13C{1H} NMR spectrum (C6D6, 125 MHz, 25 °C) of 3e. Figure S56: 13C DEPT135 experiment (C6D6, 125 MHz, 25 °C) for 3e. Figure S57: ^{1}H NMR spectrum (C6D6, 500 MHz, 25 °C) of 3f. Figure S58: 13C{1H} NMR spectrum (C6D6, 125 MHz, 25 °C) of 3f. * stands for residual NMR solvent signals. Figure S59: ^{1}H NMR spectrum (C6D6, 500 MHz, 25 °C) of 3g. *stands for residual NMR solvent signal. Figure S60: 13C{1H} NMR spectrum (CD2Cl2, 100 MHz, 25 °C) of 3g. Figure S61: ^{1}H NMR spectrum (C6D6, 400 MHz, 25 °C) of 3h. * stands for residual NMR solvent signal. Figure S62. 13C{1H} NMR spectrum (C6D6, 100 MHz, 25 °C) of 3h. Figure S63: ^{1}H NMR spectrum (C6D6, 100 MHz, 25 °C) of 3k. Figure S64: 13C{1H} NMR spectrum (C6D6, 100 MHz, 25 °C) of 3k. Figure S65: ^{1}H NMR spectrum (tol-d8, 500 MHz, 50 °C) of the ion-pair **4c**-MeB(C_6F_5)$_3$. Figure S66: 13C{1H} NMR spectrum (tol-d8, 125 MHz, 50 °C) of the ion-pair **4c**-MeB(C_6F_5)$_3$. Figure S67: ^{1}H NMR spectrum (tol-d8, 125 MHz, 25 °C) of **5c**-MeB(C_6F_5)$_3$ after 24 h at RT. Figure S68: 11B{1H} NMR spectrum (tol-d8, 128 MHz, 25 °C) of **5c**-MeB(C_6F_5)$_3$ after 24 h at RT. Figure S69: 19F{1H} NMR Spectrum (tol-d8, 376 MHz, 25 °C) of **5c**-MeB(C_6F_5)$_3$ after 24 h at RT. Figure S70: Zoom of the aliphatic region from the 2D HSQC NMR experiment for **5c**-MeB(C_6F_5)$_3$ after 24 h at RT. Figure S71: iASAP-MS mass spectrum of **3a** (Sampling cone 40 V), Figure S72: iASAP-MS mass spectrum of **3b** (Sampling cone 40 V), Figure S73: iASAP-MS mass spectrum of **3c** (Sampling cone 40V). Figure S74: iASAP-MS mass spectrum of **3d** (Sampling cone 40 V). Figure S75: iASAP-MS mass spectrum of **3e** (Sampling cone 40 V). Figure S76: iASAP-MS mass spectrum of **3f** (Sampling cone 20V). Figure S77: iASAP-MS mass spectrum of **3g** (Sampling cone 40 V). Figure S78: iASAP-MS mass spectrum of **3i** (Sampling cone 40 V). Figure S79: Crystal structure of proligand **2a**. Figure S80: Crystal structure of proligand **2b**. Figure S81: Crystal structure of proligand **2c**. Figure S82: Crystal structure of proligand **2e**, Figure S83: Crystal structure of proligand **2f**. Figure S84: Crystal structure of proligand **2i**. Figure S85: Crystal structure of proligand **2j**. Figure S86: Crystal structure of proligand **2k**. Table S1: Summary of crystal refinement data for **2a**–**c**, **2e**. Table S1 (continued): Summary of crystal refinement data for **2f**, **2i**–**k**. Figure S87: Crystal structure of complex **3b**. Figure S88: Crystal structure of complex **3c**.CH_2Cl_2. Figure S89: Crystal structure of complex **3d**. Figure S90: Crystal structure of complex **3e**. Figure S91: Crystal structure of complex **3g**. Figure S92: Crystal structure of complexes **3h** $(C_6H_{14})_{0.5}$. Table S2: Crystal refinement data for complexes **3b**–**e**, **g**, **h (CCDC 2068317–2068330)**. Table S3: Propylene polymerization data for precatalysts **3a**–**i**. Table S4: Pentad distributions (%) and the corresponding probability parameters determined experimentally, and those simulated using a three-parameter model.

Author Contributions: J.-F.C. and E.K. designed the study and the experiments. X.D. performed the experiments and analyses. T.R. and V.D. performed XRD analyses. X.D., J.-F.C. and E.K. interpreted the experiments and wrote the manuscript. A.W., A.V. and K.D.D. helped in co-supervision of the study. All authors have read and agreed to the published version of the manuscript.

Funding: This research received no external funding.

Acknowledgments: This work was financially supported by TotalEnergies and Total Research and Technology Feluy (PhD grant to XD). We are grateful to Marie Cordier (CDIFX, Univ Rennes) for resolving the structure of **3e**. EK thanks ENSCR and the CTI group of ISCR for computational facilities.

Conflicts of Interest: The authors declare no conflict of interest.

References

1. Resconi, L.; Fritze, C. *Polypropylene Handbook*; Pasquini, N., Ed.; Hanser Publishers: Munich, Germany, 2005; pp. 107–147.
2. Fink, G.; Brintzinger, H.H. Polymerization Reactions. In *Metal-Catalysis in Industrial Organic Processes*; Chiusoli, G.P., Maitlis, P.M., Eds.; Royal Society of Chemistry: Colchester, UK, 2006; pp. 218–254.
3. Ewen, J.A.; Elder, M.J. Process and Catalyst for Producing Isotactic Polyolefins. Eurpean Patent EP0537130A1, 14 April 1993.

4. Razavi, A.; Atwood, J.L. Preparation and crystal structures of the complexes (η^5-C_5H_3Me-CMe_2-η^5-$C_{13}H_8$)MCl_2 (M = Zr or Hf): Mechanistic aspects of the catalytic formation of a syndiotactic-isotactic stereoblock-type polypropylene. *J. Organomet. Chem.* **1995**, *497*, 105–111. [CrossRef]
5. Resconi, L.; Cavallo, L.; Fait, A.; Piemontesi, F. Selectivity in Propene Polymerization with Metallocene Catalysts. *Chem. Rev.* **2000**, *100*, 1253–1346. [CrossRef]
6. Alt, H.G.; Köppl, A. Effect of the nature of metallocene complexes of group IV metals on their performance in catalytic ethylene and propylene polymerization. *Chem. Rev.* **2000**, *100*, 1205–1222. [CrossRef]
7. Miller, S.A.; Bercaw, J.E. Isotactic−Hemiisotactic Polypropylene from C_1-Symmetric *ansa*-Metallocene Catalysts: A New Strategy for the Synthesis of Elastomeric Polypropylene. *Organometallics* **2002**, *21*, 934–945. [CrossRef]
8. Miller, S.A.; Bercaw, J.E. Highly Stereoregular Syndiotactic Polypropylene Formation with Metallocene Catalysts via Influence of Distal Ligand Substituents. *Organometallics* **2004**, *23*, 1777–1789. [CrossRef]
9. Miller, S.A.; Bercaw, J.E. Mechanism of Isotactic Polypropylene Formation with C_1-Symmetric Metallocene Catalysts. *Organometallics* **2006**, *25*, 3576–3592. [CrossRef]
10. Castro, L.; Kirillov, E.; Miserque, O.; Welle, A.; Haspeslagh, L.; Carpentier, J.-F.; Maron, L. Are Solvent and Dispersion Effects Crucial in Olefin Polymerization DFT Calculations? Some Insights from Propylene Coordination and Insertion Reactions with Group 3 and 4 Metallocenes. *ACS Catal.* **2015**, *5*, 416–425. [CrossRef]
11. Castro, L.; Theurkauff, G.; Vantomme, A.; Welle, A.; Haspeslagh, L.; Brusson, J.-M.; Maron, L.; Carpentier, J.-F.; Kirillov, E. A theoretical outlook on the stereoselectivity origins of isoselective zirconocene propylene polymerization catalysts. *Chem. Eur. J.* **2018**, *24*, 10784–10792. [CrossRef] [PubMed]
12. Kirillov, E.; Carpentier, J.-F. {Cyclopentadienyl/Fluorenyl}-Group 4 ansa-Metallocene Catalysts for Production of Tailor-Made Polyolefins. *Chem. Rec.* **2021**, *21*, 357–375. [CrossRef]
13. Schoebel, A.; Herdtweck, E.; Parkinson, M.; Rieger, B. Ultra-Rigid Metallocenes for Highly Iso- and Regiospecific Polymerization of Propene: The Search for the Perfect Polypropylene Helix. *Chem. Eur. J.* **2012**, *18*, 4174–4178. [CrossRef]
14. Tranchida, D.; Mileva, D.; Resconi, L.; Rieger, B.; Schoebel, A. Molecular and Thermal Characterization of a Nearly Perfect Isotactic Poly(propylene). *Macromol. Chem. Phys.* **2015**, *216*, 2171–2178. [CrossRef]
15. Machat, M.R.; Lanzinger, D.; Poethig, A.; Rieger, B. Ultrarigid Indenyl-based Hafnocene Complexes for the Highly Isoselective Polymerization of Propene: Tunable Polymerization Performance Adopting Various Sterically Demanding 4-Aryl Substituents. *Organometallics* **2017**, *36*, 399–408. [CrossRef]
16. Machat, M.R.; Jandle, C.; Rieger, B. Titanocenes in Olefin Polymerization: Sustainable Catalyst System or an Extinct Species? *Organometallics* **2017**, *36*, 1408–1418. [CrossRef]
17. Izmer, V.V.; Lebedev, A.Y.; Kononovich, D.S.; Borisov, I.S.; Kulyabin, P.S.; Goryunov, G.P.; Uborsky, D.V.; Canich, J.A.M.; Voskoboynikov, A.Z. *Ansa*-Metallocenes Bearing 4-(N-Azolyl)-2- methylindenyl and Related Ligands: Development of Highly Isoselective Catalysts for Propene Polymerization at Higher Temperatures. *Organometallics* **2019**, *38*, 4645–4657. [CrossRef]
18. Kulyabin, P.S.; Goryunov, G.P.; Sharikov, M.I.; Izmer, V.V.; Vittoria, A.; Budzelaar, P.H.M.; Busico, V.; Voskoboynikov, A.Z.; Ehm, C.; Cipullo, R.; et al. *ansa*-Zirconocene Catalysts for Isotactic-Selective Propene Polymerization at High Temperature: A Long Story Finds a Happy Ending. *J. Am. Chem. Soc.* **2021**, *143*, 7641–7647. [CrossRef] [PubMed]
19. Desert, X.; Proutiere, F.; Welle, A.; Den Dauw, K.; Vantomme, A.; Miserque, O.; Brusson, J.-M.; Carpentier, J.-F.; Kirillov, E. Zirconocene-catalyzed polymerization of α-olefins: When intrinsic higher activity is flawed by rapid deactivation. *Organometallics* **2019**, *38*, 2664–2673. [CrossRef]
20. Spaleck, W.; Kuber, F.; Winter, A.; Rohrmann, J.; Bachmann, B.; Antberg, M.; Dolle, V.; Paulus, E.F. The influence of aromatic substituents on the polymerization behavior of bridged zirconocene catalysts. *Organometallics* **1994**, *13*, 954–963. [CrossRef]
21. Razavi, A.; Bellia, V.; Brauwer, Y.D.; Hortmann, K.; Peters, L.; Sirole, S.; Belle, S.V.; Thewalt, U. Syndiotactic-and Isotactic Specific Bridged Cyclopentadienyl-Fluorenyl Based Metallocenes; Structural Features, Catalytic Behavior. *Macromol. Chem. Phys.* **2004**, *205*, 347–356. [CrossRef]
22. Razavi, A.; Bellia, V.; Baekelmans, D.; Slawinsky, M.; Sirol, S.; Peters, L.; Thewalt, U. Chain "stationary" insertion mechanism and production of isotactic polypropylene with C_1-symmetric catalyst systems. *Kinet. Catal.* **2006**, *47*, 257–267. [CrossRef]
23. Tomasi, S.; Razavi, A.; Ziegler, T. Stereoregularity, Regioselectivity, and Dormancy in Polymerizations Catalyzed by C_1-Symmetric Fluorenyl-Based Metallocenes. A Theoretical Study Based on Density Functional Theory. *Organometallics* **2009**, *28*, 2609–2618. [CrossRef]
24. Wondimagegn, T.; Wang, D.; Razavi, A.; Ziegler, T. In Silico Design of C_1- and C_s-Symmetric Fluorenyl-Based Metallocene Catalysts for the Synthesis of High-Molecular-Weight Polymers from Ethylene/Propylene Copolymerization. *Organometallics* **2009**, *28*, 1383–1390. [CrossRef]
25. Kirillov, E.; Marquet, N.; Razavi, A.; Belia, V.; Hampel, F.; Roisnel, T.; Gladysz, J.A.; Carpentier, J.-F. New C_1-Symmetric Ph_2C-Bridged Multisubstituted *ansa*-Zirconocenes for Highly Isospecific Propylene Polymerization: Synthetic Approach via Activated Fulvenes. *Organometallics* **2010**, *29*, 5073–5082. [CrossRef]
26. Kirillov, E.; Marquet, N.; Bader, M.; Razavi, A.; Belia, V.; Hampel, F.; Roisnel, T.; Gladysz, J.A.; Carpentier, J.-F. Chiral-at-*ansa*-Bridged Group 4 Metallocene Complexes {(R^1R^2C)-(3,6-t-Bu_2Flu)(3-R^3-5-Me-C_5H_2)}MCl_2: Synthesis, Structure, Stereochemistry, and Use in Highly Isoselective Propylene Polymerization. *Organometallics* **2011**, *30*, 263–272. [CrossRef]

27. Bader, M.; Marquet, N.; Kirillov, E.; Roisnel, T.; Razavi, A.; Lhost, O.; Carpentier, J.-F. Old and New C_1-Symmetric Group 4 Metallocenes {(R^1R^2C)-($R^{2'}R^{3'}R^{6'}R^{7'}$-Flu)(3-R^3-5-R^4-C_5H_2)}$ZrCl_2$: From Highly Isotactic Polypropylenes to Vinyl End-Capped Isotactic-Enriched Oligomers. *Organometallics* **2012**, *31*, 8375–8387. [CrossRef]
28. Theurkauff, G.; Bader, M.; Marquet, N.; Bondon, A.; Roisnel, T.; Guegan, J.-P.; Amar, A.; Boucekkine, A.; Carpentier, J.-F.; Kirillov, E. Discrete ionic complexes of highly isoselective zirconocenes. solution dynamics, trimethylaluminum adducts, and implications in propylene polymerization. *Organometallics* **2016**, *35*, 258–276. [CrossRef]
29. Theurkauff, G.; Bondon, A.; Dorcet, V.; Carpentier, J.-F.; Kirillov, E. Heterobi- and -trimetallic Ion Pairs of Zirconocene-Based Isoselective Olefin Polymerization Catalysts with $AlMe_3$. *Angew. Chem. Int. Ed.* **2015**, *127*, 6343–6346. [CrossRef]
30. Chen, Y.-X.; Rausch, M.D.; Chien, J.C.W. Silylene-bridged fluorenyl-containing ligands and zirconium complexes with C_1 and C_s symmetry: General synthesis and olefin polymerization catalysis. *J. Organomet. Chem.* **1995**, *497*, 1–9. [CrossRef]
31. Patsidis, K.; Alt, H.G.; Milius, W.; Palackal, S.J. The synthesis, characterization and polymerization behavior of ansa cyclopentadienyl fluorenyl complexes; the X-ray structures of the complexes [($C_{13}H_8$)SiR_2(C_5H_4)]$ZrCl_2$ (R = Me or Ph). *J. Organomet. Chem.* **1996**, *509*, 63–71. [CrossRef]
32. Inazawa, S.; Okumura, Y.; Ono, M.; Sakuragi, T. Catalyst for Polyolefin Production and Process for Producing Polyolefin. International Patent WO1997040075A1, 30 October 1997.
33. Izmer, V.V.; Agarkov, A.Y.; Nosova, V.M.; Kuz'mina, L.G.; Howard, J.A.K.; Beletskaya, I.P.; Voskoboynikov, A.Z. *ansa*-Metallocenes with a Ph_2Si bridge: Molecular structures of $HfCl_2$[Ph_2Si(η^5-$C_{13}H_8$)(η^5-C_5H_4)] and $HfCl_2$[Ph_2Si($C_{13}H_9$)(η^5-C_5H_4)]$_2$. *J. Chem. Soc. Dalton Trans.* **2001**, 1131–1136. [CrossRef]
34. Nifant'ev, I.E.; Ivchenko, P.V.; Bagrov, V.V.; Okumura, Y.; Elder, M.; Churakov, A.V. Asymmetric *ansa*-Zirconocenes Containing a 2-Methyl-4-aryltetrahydroindacene Fragment: Synthesis, Structure, and Catalytic Activity in Propylene Polymerization and Copolymerization. *Organometallics* **2011**, *30*, 5744–5752. [CrossRef]
35. Ivchenko, N.B.; Ivchenko, P.V.; Nifant'ev, I.E.; Bagrov, V.V.; Kuz'mina, L.G. Synthesis of bis-cyclopentadienyl compounds with a 9,9-fluorenylidene bridge. Crystal andmolecular structure of [μ-9,9-Flu(η^5-Cp)$_2$]$ZrCI_2$. *Russ. Chem. Bull.* **2000**, *49*, 1287–1291. [CrossRef]
36. Irwin, L.J.; Reibenspies, J.H.; Miller, S.A. Synthesis and characterization of sterically expanded *ansa*-η^1-fluorenyl-amido complexes. *Polyhedron* **2005**, *24*, 1314–1324. [CrossRef]
37. Drago, D.; Pregosin, P.S.; Razavi, A. ^{13}C NMR Studies on Zr(*ansa*-Fluorenyl) Complexes. Molecules with Flexible Bonding Modes. *Organometallics* **2000**, *19*, 1802–1805. [CrossRef]
38. Razavi, A.; Thewalt, U. Preparation and crystal structures of the complexes (η^5-C_5H_3TMS–CMe_2–η^5-$C_{13}H_8$)MCl_2 and [3,6-di^{t}But$C_{13}H_6$–$SiMe_2$–N^{t}Bu]MCl_2 (M=Hf, Zr or Ti): Mechanistic aspects of the catalytic formation of a isotactic–syndiotactic stereoblock-type polypropylene. *J. Organomet. Chem.* **2001**, *621*, 267–276. [CrossRef]
39. Razavi, A.; Thewalt, U. Site selective ligand modification and tactic variation in polypropylene chains produced with metallocene catalysts. *Coord. Chem. Rev.* **2006**, *250*, 155–169. [CrossRef]
40. Won, Y.C.; Kwon, H.Y.; Lee, B.Y.; Park, Y.-W. Fulvene having substituents only on 1-, 4-, and 6-positions: A key intermediate for novel ansa-metallocene complexes. *J. Organomet. Chem.* **2003**, *677*, 133–139. [CrossRef]
41. Yu, Y.; Busico, V.; Budzelaar, P.H.M.; Vittoria, A.; Cipullo, R. Of poisons and antidotes in polypropylene catalysis. *Angew. Chem. Int. Ed.* **2016**, *55*, 8590–8594. [CrossRef] [PubMed]
42. Prosenc, M.-H.; Britzinger, H.-H. Zirconium−Alkyl Isomerizations in Zirconocene-Catalyzed Olefin Polymerization: A Density Functional Study. *Organometallics* **1997**, *16*, 3889–3894. [CrossRef]
43. Rieger, B.; Mu, X.; Mallin, D.T.; Rausch, M.D.; Chien, J.C.W. Degree of Stereochemical Control of *rac*-Et[Ind]$_2$$ZrCl_2$/MAO Catalyst and Properties of Anisotactic Polypropylenes. *Macromolecules* **1990**, *23*, 3559–3568. [CrossRef]
44. Carvill, A.; Zetta, L.; Zannoni, G.; Sacchi, M.C. *ansa*-Zirconocene-Catalyzed Solution Polymerization of Propene: Influence of Polymerization Conditions on the Unsaturated Chain-End Groups. *Macromolecules* **1998**, *31*, 3783–3789. [CrossRef]
45. Shiono, T.; Azad, S.M.; Ikeda, T. Copolymerization of atactic polypropene macromonomer with propene by an isospecific metallocene catalyst. *Macromolecules* **1999**, *32*, 5723–5727. [CrossRef]
46. Kawahara, N.; Kojoh, S.; Matsuo, S.; Kaneko, H.; Matsugi, T.; Toda, Y.; Mizuno, A.; Kashiwa, N. Study on chain end structures of polypropylenes prepared with different symmetrical metallocene catalysts. *Polymer* **2004**, *45*, 2883–2888. [CrossRef]
47. Quevedo-Sanchez, B.; Nimmons, J.F.; Coughlin, E.B.; Henson, M.A. Kinetic modeling of the effect of MAO/Zr ratio and chain transfer to aluminum in zirconocene catalyzed propylene polymerization. *Macromolecules* **2006**, *39*, 4306–4316. [CrossRef]
48. Ciancaleoni, G.; Fraldi, N.; Budzelaar, P.H.M.; Busico, V.; Macchioni, A. Activation of a bis (phenoxy-amine) precatalyst for olefin polymerisation: First evidence for an outer sphere ion pair with the methylborate counterion. *Dalton Trans.* **2009**, 8824–8827. [CrossRef]
49. Bazinet, P.; Don Tilley, T. Octa- and Nonamethylfluorenyl Complexes of Zirconium(IV): Reactive Hydride Derivatives and Reversible Hydrogen Migration between the Metal and the Fluorenyl Ligand. *Organometallics* **2009**, *28*, 2285–2293. [CrossRef]